

1 **REVISION 2**

2  
3 **Chromium influence on Mg-Al intracrystalline exchange in spinels and**  
4 **geothermometric implications**

5  
6 FERDINANDO BOSI AND GIOVANNI B. ANDREOZZI

7  
8 Dipartimento di Scienze della Terra, Sapienza Università di Roma, Piazzale Aldo Moro 5, I-00185 Roma, Italy  
9

10  
11  
12 **ABSTRACT**

13 Flux-grown spinel crystals belonging to the  $\text{MgAl}_2\text{O}_4$ - $\text{MgCr}_2\text{O}_4$  spinel series were  
14 investigated in order to reveal the effects of Cr substituting for Al on cation distribution and  
15 their influence on Mg-Al intracrystalline exchange. Samples were structurally and chemically  
16 characterized by single-crystal X-ray diffraction and electron microprobe, and cation  
17 distribution was obtained with a tested optimization model for site populations. The results  
18 evidenced that the contribution of the tetrahedral bond distance to the unit-cell parameter is  
19 smaller than that of the octahedral bond distance, which is driven by the substitution of Cr for  
20 Al. Moreover, the influence that Cr exerts on Mg-Al order-disorder intersite exchange is non-  
21 linear along the whole series.

22 The comparison between the cation distributions derived from crystal-chemical data  
23 and the O'Neill-Navrotsky thermodynamic model (with  $\alpha_{\text{Mg-Al}} = 23 \text{ kJmol}^{-1}$  and  $\beta_{\text{Mg-Al}} = 13$   
24  $\text{kJmol}^{-1}$ ) shows large discrepancies, which can be reconciled assuming  $\alpha_{\text{Mg-Al}}$  values variable  
25 from  $23 \text{ kJmol}^{-1}$  to  $100 \text{ kJmol}^{-1}$  as a function of Cr. This suggests that, irrespective of  
26 temperature, the Al ordering at the octahedrally-coordinated site increases with increasing Cr  
27 substitution for Al. The geothermometric implications of the present study point out that  
28 closure temperatures, calculated from a well-tested intersite geothermometer, are reliable for  
29 spinels with magnesiochromite component smaller than 85%, i.e.,  $\text{Cr}/(\text{Cr}+\text{Al}) < 0.85$ , whereas  
30 spinels with larger magnesiochromite component yield unreliable closure temperature.

31  
32

33

34

## INTRODUCTION

35

36

37

38

39

Mineral species with spinel-type structure are diffuse in a wide range of geological environments, from upper mantle to crust, crystallizing in various physico-chemical conditions. Their importance as petrogenetic indicators and for oxygen thermobarometry has been widely recognized and has prompted extensive studies (e.g., Ghiorso and Sack 1991; Righter et al. 2006; Papike et al. 2015).

40

41

42

43

44

45

46

47

48

49

50

51

52

53

54

55

56

57

58

59

60

Oxide spinels have formula  $AB_2O_4$  where the letter A and B represent either divalent and trivalent cations or, less frequently, tetravalent and divalent cations, respectively. The spinel structure is described, in the space group  $Fd\bar{3}m$ , as a slightly distorted cubic close-packed array of oxygen atoms, in which A and B cations are distributed over 1/8 of the tetrahedral (T) and 1/2 of the octahedral (M) coordinated sites: ( $8a$  and  $16d$  Wyckoff notation, respectively). The unit cell ( $a$ ) contains 32 oxygen atoms (at fractional coordinates  $u, u, u$ ). Two extreme cation distributions are possible in spinel: normal ( $i = 0$ ) and inverse ( $i = 1$ ), resulting in the formula  ${}^T(A_{1-i}B_i){}^M(A_iB_{2-i})O_4$ , where the letter  $i$  represents the inversion parameter, that is the number of B cations at the T site. This  $i$  parameter is temperature-dependent and increases in normal spinels from ca. 0 to ca. 0.35, whereas it decreases in inverse spinels from ca. 1 to ca. 0.70 (Nell et al. 1989; O'Neill et al. 1992; Redfern et al. 1999; Andreozzi et al. 2000). The  $i$  value is also dependent on spinel composition, oxygen fugacity and crystallization kinetics (e.g., Andreozzi et al. 2001a,b; Andreozzi and Princivalle 2002; Nestola et al. 2007, 2009; Perinelli et al. 2014; Papike et al. 2015). In addition, cation site preference has to be taken into account when analyzing cation distribution in spinels. For example,  $Cr^{3+}$ ,  $V^{3+}$  and  $Ti^{4+}$  strongly prefer the M site; Al and  $Cu^{2+}$  exhibit preference for M but are available to partly invert at the T site at high temperature;  $Fe^{3+}$  has no preference; Mg,  $Fe^{2+}$ ,  $Mn^{2+}$  and  $Co^{2+}$  exhibit preference for the T site but can also partly invert at the M site at high temperature; Zn only occupies the T site (e.g., Lucchesi et al. 1998a; Andreozzi et al. 2001a; Andreozzi and Lucchesi 2002; Bosi et al. 2008, 2010, 2012; 2016; Hålenius et al. 2007; Fregola et al. 2012; D'Ippolito et al. 2012).

61

62

63

64

65

In spinel, at high temperature most of the cations are partially disordered between the T and M sites due to role of entropy in controlling order-disorder in these systems and as the structure is somewhat more accommodating of the different-sized cations than at low temperature. During the cooling path, on the other hand, there is a continuous cation ordering, which firstly follows an equilibrium path and then progressively deviates from it.

66 The temperature of apparent equilibration corresponding to the quenched-in ordering state,  
67 that is, the temperature at which the rate of exchange slows to the point where the change is  
68 no longer detectable, is defined as closure temperature  $T_c$  (Ganguly 1982). This process  
69 implies that the cation ordering also relies on the rate at which spinel cooled, and is a track of  
70 thermal history of host rock. A lot of studies focused on Mg-Al intracrystalline order-disorder  
71 relationships, their dependence on equilibrium temperature, cooling history and composition,  
72 with the aim of using Mg-Al rich-spinels for geothermometric purposes (e.g., Princivalle et al.  
73 1989; Peterson et al. 1991; Millard et al. 1992; Della Giusta et al. 1996; Princivalle et al.  
74 1999; Androzzzi et al. 2000; Androzzzi and Princivalle 2002). This intersite geothermometer  
75 is analytically challenging, because requires the determination of the site distribution of Mg  
76 and Al, which is (at least) temperature- and time-dependent. In fact, the higher the  
77 temperature, the higher the disorder of Mg and Al over T and M; vice versa, during crystal  
78 cooling Mg and Al progressively orders at T and M, respectively. As stated above, the  
79 ordering process stops at  $T_c$  and depends on cooling rate: slow cooling allows a strong Mg-Al  
80 intracrystalline ordering in spinel and the geothermometer calculates low  $T_c$ , whereas fast  
81 cooling preserves the disordered state and consequently gives higher  $T_c$  (e.g., Princivalle et  
82 al. 1989, 1999; Della Giusta et al. 1996; Lucchesi et al. 1998b, 2010).

83 Cr-bearing spinels represent 14% of all mineral inclusions in cratonic diamonds (e.g.,  
84 Stachel and Harris 2008, Lenaz et al. 2009; Nestola et al. 2014), and are often among the first  
85 phases that crystallize from a wide variety of mafic-ultramafic igneous rock types and tectonic  
86 environments (e.g., Irvine 1965, 1967; Barnes and Roeder 2001; Lenaz et al. 2014a).  
87 Therefore, they may preserve important records of the geological conditions in which they  
88 formed in the crust and upper mantle, and understanding how to decipher those records is  
89 extremely important. However, in Mg-Al-Cr-spinels, the marked preference of Cr for the  
90 octahedral environment strongly influences both spinel crystal-chemistry and calculated  $T_c$  by  
91 affecting the site distribution of Mg and Al (Lavina et al. 2003). Moreover, natural Mg-Al-Cr-  
92 spinels often contain other chemical constituents such as  $\text{Fe}^{2+}$  and  $\text{Fe}^{3+}$  that may hinder the  
93 influence of Cr on both cation ordering and  $T_c$  (Martignago et al. 2003). It is therefore crucial  
94 to test geothermometric exchanges studying spinel samples along the Fe-free binary series  
95 spinel *sensu stricto* (s.s.)-magnesiochromite ( $\text{MgAl}_2\text{O}_4$ - $\text{MgCr}_2\text{O}_4$ ).

96 In the present study, the  $\text{MgAl}_2\text{O}_4$ - $\text{MgCr}_2\text{O}_4$  spinel substitution series will be  
97 investigated in order to reveal the crystal-chemical effects of Cr substitution for Al and their  
98 influence on Mg-Al intracrystalline exchange. Flux-grown synthetic crystals, already studied  
99 by optical absorption spectroscopy in Hålenius et al. (2010), will be structurally and

100 chemically characterized by single-crystal X-ray diffraction and electron microprobe, cation  
101 distribution will be obtained with a tested optimization model for site populations, and  $T_c$  will  
102 be finally calculated with the geothermometer equation of Princivalle et al. (1999). The  
103 approach adopted will allow the definition of the compositional range where this  
104 geothermometer applies when the  $MgCr_2O_4$  component increases.

105

106

107

## EXPERIMENTAL METHODS

### 108 **Synthesis**

109 A flux-growth method with  $Na_2B_4O_7$  used as flux compound was used to obtain single  
110 crystals along the binary join spinel s.s.-magnesiochromite. Analytical grade  $MgO$ ,  $Al(OH)_3$   
111 and  $Cr_2O_3$  were dehydrated and dried at elevated temperatures before mixing with  $Na_2B_4O_7$ .  
112 The starting materials were transferred to Pt/Au (5%) crucibles and covered by a Pt lid.  
113 Thermal runs consisted of 24 h at 1200 °C followed by a slow decrease to 900 °C at a  
114 controlled cooling rate of 4 °C/h. After shutting off the power to the heating elements and  
115 removing crucibles from the furnace a rapid cooling to room temperature was obtained.  
116 Successful runs consisted of octahedral spinel crystals, borate needles, and occasional  
117 eskolaite ( $\alpha$ - $Cr_2O_3$ ) embedded in a borate-rich glass. The glass phase and borate crystals were  
118 dissolved in warm diluted HCl. The recovered spinel single crystal have typical size in the  
119 range 200-300  $\mu m$ . The largest, ruby-red, gem-quality crystals were obtained for Cr-poor  
120 compositions, intermediate compositions yielded sub-regular crystals, but smaller, black  
121 octahedra were also obtained close to magnesiochromite end member.

122

### 123 **Single-crystal structural refinement**

124 The examined samples constitute a set of nine hand-picked spinel single crystals. For X-  
125 ray data collection two single-crystal diffractometers were used (Siemens P4 and APEX-II).  
126 In detail, six out of nine crystal-fragments were mounted on a Bruker Siemens P4 automated  
127 four-circle diffractometer, equipped with a point detector. Unit-cell parameters were  
128 measured, at 293 K, by centering 52 reflections (13 independent and their Friedel pairs, on  
129 both sides of the direct beam), in the range 85-95°  $2\theta$ , with  $Mo-K\alpha_1$  radiation (0.70930 Å).  
130 Intensity data were collected, at 293 K, using  $MoK\alpha$  radiation (0.71073 Å) monochromatized  
131 by a flat graphite crystal in the 3-95°  $2\theta$  range with the  $\omega$ -scan method and at a fixed scan  
132 range (2.4°). One-eighth of the reciprocal space was examined. The scan speed was variable  
133 (2.93-29.3°/min), depending on reflection intensity, as estimated through pre-scans. The

134 background was measured with a stationary counter and crystal at the beginning and end of  
135 each scan, in both cases for half the scan time. Three standard reflections were monitored  
136 every 47 measurements. Data reduction was performed with the SHELXTL-PC program  
137 package. Intensities were corrected for polarization and Lorentz effects. Absorption correction  
138 was accomplished with a semi-empirical method (North et al. 1968). Three out of nine  
139 crystal-fragments were mounted on a Bruker KAPPA APEX-II diffractometer, equipped with  
140 a CCD area detector ( $6.2 \times 6.2 \text{ cm}^2$  active detection area,  $512 \times 512$  pixels) and a graphite  
141 crystal monochromator, using  $\text{MoK}\alpha$  radiation from a fine-focus sealed X-ray tube. The  
142 sample-to-detector distance was 4 cm. More than 5000 exposures per sample were measured  
143 (step =  $0.2^\circ$ , time/step = 10 s) covering the full reciprocal sphere with an average redundancy  
144 of about 20. Final unit-cell parameters were refined by using the Bruker AXS SAINT  
145 program from about 2000 (about 1200 for sample MgCr5c) recorded reflections with  $I > 10$   
146  $\sigma_I$  in the range  $8^\circ < 2\theta < 90^\circ$  ( $72^\circ$  for sample MgCr5c). The intensity data were processed and  
147 corrected for Lorentz, polarization and background effects with the APEX2 software program  
148 of Bruker AXS. The data were corrected for absorption using multi-scan method (SADABS),  
149 leading to a significant improvement in  $R_{\text{int}}$ . No violation of  $Fd\bar{3}m$  symmetry was noted.

150 Structure refinement was done with the SHELXL-2013 program (Sheldrick 2013). All  
151 reflections were used in the refinement. Variable parameters during the structural refinement  
152 were: overall scale factor, oxygen coordinate, site-scattering values, atomic-displacement  
153 parameters, and extinction parameter. In the final stage of the refinement, the extinction  
154 parameter was removed from the variables of sample MgCr5c, because its value refined to  
155 zero. Setting the origin at  $\bar{3}m$ , initial atomic positions for oxygen atoms were taken from  
156 Hålenius and Bosi (2014). The T site was modeled with Mg and the M site with Al vs. Cr  
157 (except for crystal MC02bb, which was modeled considering only  $^{\text{M}}\text{Al}$  due to the small Cr  
158 concentrations). Convergence was attained when the shifts in all refined parameters were less  
159 than their estimated standard deviation. A further refinement with chemical constraints was  
160 done for CIF (on deposit<sup>1</sup>) by modelling the T site cation occupancy of crystals MC02bb and  
161 MC02de with the  $^{\text{T}}\text{Mg}$  and  $^{\text{T}}\text{Al}$  fixed to the value obtained from the structural formula. The  
162 results are statistically equal to those reported in Table 1, which summarizes structural  
163 parameters and refinement details.

164

## 165 **Electron microprobe analysis**

166 The same crystals as used for X-ray data collection were mounted on a glass slide and  
167 polished for electron microprobe analysis on a Cameca SX50 instrument equipped with four  
168 wavelength dispersive spectrometers (WDS mode) and operated at an accelerating potential of  
169 15 kV and a sample current of 15 nA, with an incident beam diameter of ca. 1  $\mu\text{m}$ . No less  
170 than 10 spot analyses for each sample were performed to obtain the average chemical  
171 compositions and to estimate compositional homogeneity. Synthetic standards used were  
172 periclase (Mg), corundum (Al) and metallic Cr. For raw data reduction, the PAP computer  
173 program was applied (Pouchou and Pichoir 1984). Spinel formulae were calculated on the  
174 basis of 4 oxygen atoms and 3 cations per formula unit. The resulting atomic fractions (atoms  
175 per formula unit, apfu) are well supported by the match between number of electrons per  
176 formula unit derived from chemical and structural analysis (Table 2).

177

### 178 **Cation distribution**

179 The intersite cation distribution was obtained by minimizing the residuals between  
180 calculated and observed chemical-structural data by using a least-squares approach. The  
181 minimized function is:

$$182 \quad F(X_i) = \frac{1}{n} \sum_{j=1}^n \left( \frac{O_j - C_j(X_i)}{\sigma_j} \right)^2$$

183 where  $O_j$  is the observed quantity,  $\sigma_j$  its standard error,  $X_i$  the variables, i.e., cation fractions at  
184 the T and M sites, and  $C_j(X_i)$  the same quantity as  $O_j$  calculated by means of  $X_i$  parameters.  
185 The  $nO_j$  quantities taken into account were:  $a$ - and  $u$ -parameter, T-O and M-O bond distances,  
186 mean atomic number of T and M sites, total atomic fractions derived from electron-  
187 microprobe analyses, constraints relative to the formula electroneutrality (8 positive and 8  
188 negative charges) and site population (T = 1.000 and M = 2.000). The M-O and T-O bond  
189 distances were calculated as the linear contribution of each cation multiplied by its ideal bond  
190 distance reported by Lavina et al. (2002):  ${}^T\text{Mg-O} = 1.966 \text{ \AA}$ ,  ${}^M\text{Mg-O} = 2.082 \text{ \AA}$ ,  ${}^T\text{Al-O} =$   
191  $1.774 \text{ \AA}$ ,  ${}^M\text{Al-O} = 1.908 \text{ \AA}$ ,  ${}^M\text{Cr}^{3+}\text{-O} = 1.995 \text{ \AA}$ . More details about the minimization  
192 procedure may be found in Lavina et al. (2002). Due to crystal-field stabilization energy, a  
193 marked octahedrally coordinated site preference is expected for  $\text{Cr}^{3+}$ , thus it was constrained  
194 to occur at the M site. The calculated parameters fit the observed ones within  $2\sigma$  in 95% of  
195 cases (Table 3, on deposit). The results of optimized cation distributions are reported as  
196 structural formulae in Table 4.

197

198

199

## RESULTS AND DISCUSSION

### 200 **Crystal structure**

201 Crystal structure of Cr-bearing spinels at environmental conditions is commonly  
202 described on the basis of  $Fd\bar{3}m$  space group. The end member  $MgCr_2O_4$  exhibits a first-order  
203 phase transition at 12.5 K with a pronounced peak in heat capacity coinciding with the phase  
204 transition from cubic to tetragonal symmetry ( $I4_1/amd$  space group; Ehrenberg et al. 2002).  
205 Moreover, a post-spinel  $MgCr_2O_4$  orthorhombic phase,  $Bbmm$  space group, was recently  
206 synthesized at 23 GPa and 1600 °C (Bindi et al. 2014) and found in ultrahigh-pressure  
207 chromitites (Ishii et al. 2015).

208 Previously studies also stated that the structure of Cr-rich spinels at environmental  
209 conditions may be better described by the space group  $F\bar{4}3m$  (Grimes 1971; Sickafus et al.  
210 1999) due to the displacement of Cr at the M site along the direction [111] from a  
211 centrosymmetric position to a non-centrosymmetric position, which causes a reduction in  
212 point symmetry of the M site from  $\bar{3}m$  to  $3m$ . In addition, Lutz et al. (2000) suggested that the  
213 occurrence of a less symmetric space group in Cr-rich spinels is due to the strength of the  
214 metal-metal bonds.

215 However, structure refinements of the present study, along with the results of O'Neill  
216 and Dollase (1994), Lenaz et al. (2004) and Nestola et al. (2014), fully support the occurrence  
217 of  $Fd\bar{3}m$  space group for both Cr-bearing spinels and the magnesiochromite end member.

218

### 219 **Crystal chemistry**

220 The flux-grown spinel crystals investigated are characterized by  $Cr \leftrightarrow Al$  substitution  
221 along the whole substitution series and are representative of the entire  $MgAl_2O_4$ - $MgCr_2O_4$   
222 series. The  $Cr_2O_3$  contents vary from 4.9(5) to 76.1(1) wt% (Table 2) and the corresponding  
223 magnesiochromite component from 3% to 96% (Table 4). To attain a complete picture of the  
224 structural relations along the whole series, we included crystal-chemical data of the synthetic  
225 end-member magnesiochromite  $T(Mg)^M(Cr)_2O_4$ , grown in the same conditions (Nestola et al.  
226 2014).

227 Site distribution of Mg, Al and Cr shows that the T site is mainly populated by Mg and  
228 by small amounts of Al which decrease with increasing Cr content. The M site is dominated  
229 by the substitution  $Cr \leftrightarrow Al$  and also shows small amounts of Mg which decrease with  
230 increasing Cr. Accordingly, the degree of inversion decreases from 0.23 to 0.00 with

231 increasing Cr content (Table 4). As a consequence, the distribution of Mg and Al over the T  
232 and M sites is well explained by the order-disorder reaction  ${}^M\text{Al} + {}^T\text{Mg} \leftrightarrow {}^T\text{Al} + {}^M\text{Mg}$ .

233 During the replacement of Al by Cr, the bond distances T-O and M-O linearly increase  
234 with increasing  ${}^T\text{Mg}$  and  ${}^M\text{Cr}$ , respectively, according to the equations:

235 
$$\text{T-O} = 0.1926 \cdot {}^T\text{Mg} + 1.7733, (r^2 = 0.9998);$$

236 
$$\text{M-O} = 0.0327 \cdot {}^M\text{Cr} + 1.9266, (r^2 = 0.996).$$

237 Moreover, M-O decreases with increasing inversion degree ( $i = {}^T\text{Al}$ ) according to a non-linear  
238 trend:

239 
$$\text{M-O} = 1.991 - 0.521 \cdot i + 1.146 \cdot i^2, (r^2 = 0.985),$$

240 and T-O shows a non-linear relation with Cr content ( $r^2 = 0.995$ ).

241 The unit-cell parameter increases from 8.092 Å to 8.332 Å with increasing Cr (Fig. 1)  
242 and is positively correlated with both T-O and M-O, which vary from 1.922 Å to 1.967 Å and  
243 from 1.930 Å to 1.994 Å, respectively. Therefore, the contribution of T-O to the unit-cell  
244 parameter variation is smaller than that of M-O, which is driven by the Cr variation in the  
245 spinel structure. The correlation between  $a$ -parameter and T-O and M-O bond distances is  
246 better described by a non-linear regression (Fig. 2), which non-linearity can be ascribed to the  
247 occurrence of a non-linear relation between  $i$  and Cr content (see below). These non-linear  
248 trends can be better explained by using the parameter  ${}^T\text{Al}/\text{Al}_{\text{tot}}$  [=  $(1 + {}^T\text{Al}/{}^M\text{Al})$ ] that  
249 represents the availability of Al to be inverted with Mg, when Cr increases. Far from being  
250 constant, the parameter  ${}^T\text{Al}/\text{Al}_{\text{tot}}$  shows a decreasing trend along the studied series, with a  
251 further drop for magnesiochromite component higher than 80% (Fig. 3). Notably, a constant  
252 value of  ${}^T\text{Al}/\text{Al}_{\text{tot}}$  would account for a constant T-site preference of Al along the whole series,  
253 whereas decreasing values at increasing Cr contents suggest a minor tetrahedral affinity of Al.  
254 Hence, the trend observed in Figure 3 represents the influence of Cr on Mg-Al intersite  
255 exchange at any given equilibration temperature or thermal pathway, that is, irrespective of  
256 temperature. Moreover, the Cr influence on Mg-Al intersite exchange may also be invoked to  
257 explain the inconsistencies observed by Lavina et al. (2003) in modelling cation distribution  
258 and cooling rates of natural Cr-bearing spinels.

259

### 260 **Thermodynamics of Mg-Al intersite exchange in presence of Cr**

261 The intracrystalline cation distribution of the present spinel s.s.-magnesiochromite series was  
262 tentatively modeled by the general thermodynamic model for spinel binary substitution series  
263 proposed by O'Neill and Navrotsky (1984), which was proved to be adequate for modeling  
264 cation distribution as a function of temperature in spinels of different composition (e.g.,

265 Waerenborgh et al. 1994a,b; Androzzzi et al. 2001a; Androzzzi and Lucchesi 2002;  
266 Martignago et al. 2006; Princivalle et al. 2012). Applying this model to  $\text{MgAl}_2\text{O}_4$ - $\text{MgCr}_2\text{O}_4$   
267 and disregarding the Cr inversion at T, due to its strong octahedral preference, the Mg-Al  
268 intersite exchange can be modeled as a function of temperature by the order-disorder reaction  
269  ${}^{\text{M}}\text{Al} + {}^{\text{T}}\text{Mg} \leftrightarrow {}^{\text{T}}\text{Al} + {}^{\text{M}}\text{Mg}$ . Accordingly, the system of two equations, required for the general  
270 case, may be simplified as follows:

$$271 \quad -RT\ln\left[\frac{i^2}{(1-i)(2-i-2z)}\right] = \alpha_{\text{Mg-Al}} + 2\beta_{\text{Mg-Al}} i \quad (3)$$

272 where  $i = {}^{\text{T}}\text{Al}$  in apfu,  $2z =$  magnesiochromite molar content (i.e.,  $\text{Cr}_{\text{tot}}$  in apfu),  $\alpha_{\text{Mg-Al}} = 23$   
273  $\text{kJmol}^{-1}$ , and  $\beta_{\text{Mg-Al}} = 13 \text{ kJmol}^{-1}$  (Androzzzi et al. 2000). Equation (3) was solved for a range  
274 of temperatures, but  $T = 800 \text{ }^\circ\text{C}$  was eventually fixed (see below), and for  $2z$  corresponding to  
275 the Cr contents of Table 4. The resulting values of  $i$ , however, show a large deviation from  $i$   
276 values derived from the crystal-chemical data (Fig. 4a). This deviation is maximum for  
277 intermediate Cr contents. The values calculated from the thermodynamic model would also  
278 suggest that, as a consequence of the influence of Cr on Mg-Al intersite exchange, the T-site  
279 preference of Al is non-linearly enhanced along the series. However, this is opposite to what  
280 observed (Fig. 4b).

281 The O'Neill-Navrotsky model assumes that cation ordering behavior in a substitution  
282 series can be entirely predicted on the basis of the energetics of the two end members (or one  
283 end member in this case, as the other is constrained to be perfectly normal). This is seen in  
284 equation (3), where the ordering is controlled by the parameters  $\alpha$  and  $\beta$ , which are entirely  
285 constrained by the equilibrium ordering behavior in end member  $\text{MgAl}_2\text{O}_4$ . This approach,  
286 however, ignores the important energetic contributions from Al-Cr pairwise interactions, that  
287 are only present along the substitution series, and whose effects cannot possibly be predicted  
288 from the end member behavior alone. Actually, in the present case the deviation between the  
289 model and observations is maximum for intermediate Cr contents because this is where the  
290 maximum number of Al-Cr interactions occur (Fig. 4a). This issue was discussed extensively  
291 for the magnesioferrite-qandilite series in Palin and Harrison (2007) and Harrison et al.  
292 (2013), who found that the total energy of such a series can formally be expressed as a sum of  
293 pairwise cation-cation interaction parameters and chemical potentials. The atomistic approach  
294 used by Harrison et al. (2013) is rigorous and effectively describes the underlying physics of  
295 spinel order-disorder with temperature along a substitution series. However, it is complex and  
296 lacks of an analytical solution, having rather limited practical use. On the other hand, the  
297 O'Neill-Navrotsky model is relatively simple and has been successfully used in many cases.

298 Nevertheless, it has been proved unsuccessful for the magnesioferrite-qandilite series  
299 (Harrison et al. 2013) as well as for the studied spinel s.s.-magnesiocromite series as it led to  
300 cation distribution inconsistent with experimental data. In the present study, for example, for  
301 an intermediate composition such as crystal MC15ad the T-O and M-O bond distances  
302 derived from thermodynamic data were 1.9341 and 1.9681 Å, respectively, which are  
303 significantly smaller than the corresponding observed values 1.9538(9) and 1.9588(5) Å  
304 (Table 1).

305 The unique way to apply the O'Neill-Navrotsky model to the present series is varying  
306  $\alpha_{\text{Mg-Al}}$  and  $\beta_{\text{Mg-Al}}$  values in equation (3) as both  $T$  and  $i$  are known parameters. Using the  
307 inversion values of Table 4 and assuming a constant value of  $\beta_{\text{Mg-Al}} = 13 \text{ kJmol}^{-1}$  (Andreozzi  
308 et al. 2000),  $\alpha_{\text{Mg-Al}}$  values spanning from 23 to 100  $\text{kJmol}^{-1}$  along the whole series were  
309 determined (Table 4). A strong correlation was observed between  $\alpha_{\text{Mg-Al}}$  and Cr, as well as  
310 between  $\alpha_{\text{Mg-Al}}$  and  $^{\text{T}}\text{Al}/\text{Al}_{\text{tot}}$ . The latter can be described by the equation  $\alpha_{\text{Mg-Al}} = 125 - 1560$   
311  $\cdot (^{\text{T}}\text{Al}/\text{Al}_{\text{tot}}) + 5960 \cdot (^{\text{T}}\text{Al}/\text{Al}_{\text{tot}})^2$ , ( $r^2 = 0.995$ ). As  $\alpha_{\text{Mg-Al}}$  represents the difference in the site  
312 preference energies of Mg and Al, the progressively higher values here retrieved would  
313 account for an increasing preference of Al for the octahedral coordination as a function of Cr,  
314 which may be ascribed to the pairwise Al-Cr interaction.

315

### 316 **Geothermometry**

317 Della Giusta et al. (1996) and Princivalle et al. (1999) defined a geothermometric  
318 relation that allows calculation of the closure temperature for a spinel from its cation  
319 distribution. The geothermometer is based on the temperature-dependent intracrystalline  
320 exchange reaction  $^{\text{M}}\text{Al} + ^{\text{T}}\text{Mg} = ^{\text{T}}\text{Al} + ^{\text{M}}\text{Mg}$ . The closure temperature is obtained by the  
321 equation:  $T_c = 6640 [^{\text{T}}\text{Al}/\text{Al}_{\text{tot}} + 0.101(1 - ^{\text{T}}\text{Mg} - ^{\text{T}}\text{Al}) + 0.041(2 - ^{\text{M}}\text{Al} - ^{\text{M}}\text{Mg})]$ , where the  
322 coefficients should take into account the compositional influence of the other cations such as  
323 Cr. The estimated error associated with this geothermometer is  $\pm 20 \text{ }^\circ\text{C}$ .

324 Due to common occurrence and high relevance of Cr-bearing spinels in geosciences,  
325 after Princivalle et al. (1999) the geothermometer was applied to natural Cr-bearing spinels by  
326 Lavina et al. (2003), Uchida et al. (2005), Lucchesi et al. (2010), Lenaz et al. (2010; 2014b,c;  
327 2015) and Perinelli et al. (2014). All these studies validated the successful application of this  
328 single-phase geothermometer on geological evidences or against other geothermometers  
329 based on coexisting phases. None validation, however, has been done against synthetic spinel  
330 samples with increasing Cr contents under controlled temperature. The present samples were

331 grown by controlled, slow-cooling thermal runs ending at 900 °C, after that they were not  
332 quenched, but carefully removed from the vertical furnace. Due to this procedure, crystals  
333 remained in the furnace for several minutes after switching off heating elements. Due to fast  
334 Mg-Al intersite exchange kinetics between 900 and 800 °C (Andreozzi and Princivalle 2002),  
335 their closure temperature is therefore expected to be about 800 °C.

336 Applied to the present crystals with Cr content up to 1.66 apfu the geothermometer of  
337 Princivalle et al. (1999) yields  $T_c$  spanning from 768 to 824 °C, with an average value of  
338  $796 \pm 20$  °C that is consistent with the expected value of 800 °C (Fig. 5). For larger Cr  
339 contents, such as that of crystal MC50b (Cr = 1.92 apfu), the geothermometer yields  
340 unreliable  $T_c$  (637 °C), significantly lower than 800 °C. This large deviation can be ascribed  
341 to the non-linear behavior of the Mg-Al order-disorder reaction caused by Cr.

342

343

344

#### IMPLICATIONS

345 Chromium influence on Mg-Al intracrystalline exchange in spinels implies that the  
346 geothermometer of Princivalle et al. (1999) yields reliable  $T_c$  values for spinel compositions  
347 with  $Cr/(Cr+Al) < 0.85$ , whereas  $T_c$  values calculated for spinels with  $Cr/(Cr+Al) > 0.85$   
348 should be treated with caution. This finding, along with the unreliable  $T_c$  estimated for non-  
349 stoichiometric Cr-bearing spinels (Perinelli et al. 2014; Lenaz et al. 2015) put some  
350 limitations on the compositional field where this spinel geothermometer can be used, i.e., Cr  
351 contents lower than 1.70 apfu and absence of cation vacancies. The geological implications  
352 may be relevant: for example, spinels with very high Cr contents,  $Cr/(Cr+Al) > 0.85$ , are  
353 typically found as inclusions in diamonds or contained in kimberlites, komatiites, boninites  
354 and ophiolitic chromitites (e.g., Barnes and Roeder 2001). An improper use of the  
355 geothermometer of Princivalle et al. (1999) on such spinels would lead to incorrect  
356 interpretations such as lower closure temperature indicating slow cooling rate due to a slow  
357 cooling path experienced by their host rock or, alternatively, long exposure to low-to-  
358 medium-grade metamorphic conditions, which are characterized by sluggish kinetics.

359

360

361

#### ACKNOWLEDGEMENTS

362 Chemical analyses were done with the CAMECA SX50 electron microprobe of the  
363 “Istituto di Geologia Ambientale e Geoingegneria (Rome, Italy), CNR”, with the kind  
364 assistance of M. Serracino to whom the authors wish to express their gratitude. Grants from

365 Sapienza University (2013 to G.B.A. and 2014 to F.B.), and SYNTHESYS program (SE-  
366 TAF-3729 to G.B.A) are gratefully acknowledged. We thank two anonymous reviewers for  
367 their comments and K. Lilova for the efficient handling of the manuscript.

368

369

#### 370 REFERENCES CITED

371 Andreozzi, G.B. and Lucchesi, S. (2002) Intersite distribution of Fe<sup>2+</sup> and Mg in the spinel  
372 (sensu stricto)–hercynite series by single-crystal X-ray diffraction. American  
373 Mineralogist, 87, 1113–1120.

374 Andreozzi, G.B., Princivalle, F. (2002) Kinetics of cation ordering in synthetic MgAl<sub>2</sub>O<sub>4</sub>  
375 spinel. American Mineralogist, 87, 838–844.

376 Andreozzi, G.B., Princivalle, F., Skogby, H., and Della Giusta, A. (2000) Cation ordering and  
377 structural variations with temperature in MgAl<sub>2</sub>O<sub>4</sub> spinel: An X-ray single crystal  
378 study. American Mineralogist, 85, 1164–1171.

379 Andreozzi, G.B., Lucchesi, S., Skogby, H., and Della Giusta, A. (2001a) Composition  
380 dependence of cation distribution in some synthetic (Mg,Zn)(Al,Fe<sup>3+</sup>)<sub>2</sub>O<sub>4</sub> spinels.  
381 European Journal of Mineralogy, 13, 391–402.

382 Andreozzi, G.B., Hålenius, U., and Skogby, H. (2001b) Spectroscopic active <sup>IV</sup>Fe<sup>3+</sup> -<sup>VI</sup>Fe<sup>3+</sup>  
383 clusters in spinel-magnesioferrite solid solution crystals: a potential monitor for  
384 ordering in oxide spinels. Physics and Chemistry of Minerals, 28, 435–444.

385 Barnes, S.J., and Roeder, P.L. (2001) The range of spinel compositions in terrestrial mafic and  
386 ultramafic rocks. Journal of Petrology, 42, 2279–2302.

387 Bindi, L., Sirotkina, E.A., Bobrov, A.V., Irifune, T. (2014) X-ray single-crystal structural  
388 characterization of MgCr<sub>2</sub>O<sub>4</sub>, a post-spinel phase synthesized at 23 GPa and  
389 1,600°C. Journal of Physics and Chemistry of Solids, 75, 638–641.

390 Bosi, F., Hålenius, U., and Skogby, H. (2008) Stoichiometry of synthetic ulvöspinel single  
391 crystals. American Mineralogist, 93, 1312–1316.

392 Bosi, F., Hålenius, U., and Skogby, H. (2010) Crystal chemistry of the MgAl<sub>2</sub>O<sub>4</sub>-MgMn<sub>2</sub>O<sub>4</sub>-  
393 MnMn<sub>2</sub>O<sub>4</sub> system: Analysis of structural distortion in spinel- and hausmannite-type  
394 structures. American Mineralogist, 95, 602–607.

395 Bosi, F., Hålenius, U., D'Ippolito, V., and Andreozzi, G.B. (2012) Blue spinel crystals in the  
396 MgAl<sub>2</sub>O<sub>4</sub>-CoAl<sub>2</sub>O<sub>4</sub> series: II. Cation ordering over short-range and long-range  
397 scales. American Mineralogist, 97, 1834–1840.

- 398 Bosi, F., Skogby, H., Fregola, R.A., and Hålenius, U. (2016) Crystal chemistry of spinels in  
399 the system  $\text{MgAl}_2\text{O}_4$ - $\text{MgV}_2\text{O}_4$ - $\text{Mg}_2\text{VO}_4$ . *American Mineralogist*, 580–586.
- 400 D’Ippolito, V., Andreozzi, G.B., Bosi, F., and Hålenius, U. (2012) Blue spinel crystals in the  
401  $\text{MgAl}_2\text{O}_4$ - $\text{CoAl}_2\text{O}_4$  series: I. Flux growth and chemical characterization. *American*  
402 *Mineralogist*, 97, 1828–1833.
- 403 Della Giusta, A., Carbonin, S., and Ottonello, G. (1996) Temperature-dependent disorder in a  
404 natural Mg-Al- $\text{Fe}^{2+}$ - $\text{Fe}^{3+}$ -spinel. *Mineralogical Magazine*, 60, 603–616.
- 405 Ehrenberg, H., Knapp, M., Baetz, C., and Klemme, S. (2002) Tetragonal low-temperature  
406 phase of  $\text{MgCr}_2\text{O}_4$ . *Powder Diffraction*, 17, 230–233.
- 407 Fregola, R.A., Bosi, F., Skogby, S., and Hålenius, U. (2012) Cation ordering over short-range  
408 and long-range scales in the  $\text{MgAl}_2\text{O}_4$ - $\text{CuAl}_2\text{O}_4$  series. *American Mineralogist*, 97,  
409 1821–1827.
- 410 Ganguly, J. (1982) Thermodynamics, Kinetics, and Geological Applications. In *Advances in*  
411 *Physical Geochemistry*, Ed. By S.K. Saxena, Springer-Verlag.
- 412 Ghiorso, M.S. and Sack, R.O. (1991) Thermochemistry of the oxide minerals. in “Oxide  
413 minerals: petrologic and magnetic significance”, D.H. Lindsley, ed. *Mineralogical*  
414 *Society of America, Virginia*, 25, 221–262.
- 415 Grimes, N.W. (1971) Structural distortions in  $\text{MgCr}_2\text{O}_4$ . *Journal of Physics C: Solid State*  
416 *Physics*, 4, L342–L344.
- 417 Hålenius, U., and Bosi, F. (2014) Color of Mn-bearing gahnite: A first example of electronic  
418 transitions in heterovalent exchange coupled  $^{\text{IV}}\text{Mn}^{2+}$ - $^{\text{VI}}\text{Mn}^{3+}$  pairs in minerals.  
419 *American Mineralogist*, 99, 261–266.
- 420 Hålenius, U., Bosi, F., and Skogby, H. (2007) Galaxite,  $\text{MnAl}_2\text{O}_4$ , a spectroscopic standard  
421 for tetrahedrally coordinated  $\text{Mn}^{2+}$  in oxygen-based mineral structures. *American*  
422 *Mineralogist* 92, 1225–1231.
- 423 Hålenius, U., Andreozzi, G.B., and Skogby, H. (2010) Structural relaxation around  $\text{Cr}^{3+}$  and  
424 the red-green color change in the spinel (sensu stricto)-magnesiochromite  
425 ( $\text{MgAl}_2\text{O}_4$ - $\text{MgCr}_2\text{O}_4$ ) and gahnite–zincchromite ( $\text{ZnAl}_2\text{O}_4$ - $\text{ZnCr}_2\text{O}_4$ ) solid solution  
426 series. *American Mineralogist*, 95, 456–462.
- 427 Harrison, R.J., Palin, E.J., and Perks, N. (2013) A computational model of cation ordering in  
428 the magnesioferrite-qandilite ( $\text{MgFe}_2\text{O}_4$ - $\text{Mg}_2\text{TiO}_4$ ) solid solution and its potential  
429 application to titanomagnetite ( $\text{Fe}_3\text{O}_4$ - $\text{Fe}_2\text{TiO}_4$ ). *American Mineralogist*, 98, 698–  
430 708.

- 431 Irvine, T.N. (1965) Chromian spinel as a petrogenetic indicator. Part 1 Theory. Canadian  
432 Journal of Earth Science, 2, 648–672.
- 433 ——— (1967) Chromian spinel as a petrogenetic indicator. Part 2 Petrologic applications.  
434 Canadian Journal of Earth Science, 4, 71–103.
- 435 Ishii, T., Kojitani, H., Fujino, K., Yusa, H., Mori, D., Inaguma, Y., Matsushita, Y., Yamaura,  
436 K., and Akaogi, M. (2014) High-pressure high-temperature transitions in  $\text{MgCr}_2\text{O}_4$   
437 and crystal structures of new  $\text{Mg}_2\text{Cr}_2\text{O}_5$  and post-spinel  $\text{MgCr}_2\text{O}_4$  phases with  
438 implications for ultrahigh-pressure chromitites in ophiolites. American Mineralogist,  
439 100, 59–65.
- 440 Lavina, B., Salviulo, G., and Della Giusta, A. (2002) Cation distribution and structure  
441 modelling of spinel solid solutions. Physics and Chemistry of Minerals, 29, 10–18.
- 442 Lavina, B., Koneva, A., and Della Giusta, A. (2003) Cation distribution and cooling rates of  
443 Cr-substituted Mg-Al spinel from the Olkhon metamorphic complex, Russia.  
444 European Journal of Mineralogy, 15, 435–441.
- 445 Lenaz, D., Skogby, H., Princivalle, F., and Hålenius, U. (2004) Structural changes and  
446 valence states in the  $\text{MgCr}_2\text{O}_4$ - $\text{FeCr}_2\text{O}_4$  solid solution series. Physics and Chemistry  
447 of Minerals, 31, 633–642.
- 448 Lenaz, D., Logvinova, A.M., Princivalle, F., and Sobolev, N. (2009) Structural parameters of  
449 chromite included in diamond and kimberlites from Siberia: A new tool for  
450 discriminating ultramafic source. American Mineralogist, 94, 1067–1070.
- 451 Lenaz, D., De Min, A., Garuti, G., Zaccarini, F., and Princivalle, F. (2010) Crystal chemistry  
452 of Cr-spinels from the lherzolite mantle peridotite of Ronda (Spain). American  
453 Mineralogist, 95, 1323–1328.
- 454 Lenaz, D., Andreozzi, G.B., Bidyananda, M. and Princivalle, F. (2014a) Oxidation degree of  
455 chromite from Indian ophiolites: a crystal chemical and  $^{57}\text{Fe}$  Mössbauer study.  
456 Periodico di Mineralogia, 83, 241–255.
- 457 Lenaz, D., Adetunji, J. and Rollinson, H. (2014b) Determination of  $\text{Fe}^{3+}/\Sigma\text{Fe}$  ratios in chrome  
458 spinels using a combined Mössbauer and single-crystal X-ray approach: application  
459 to chromitites from the mantle section of the Oman ophiolite. Contributions to  
460 Mineralogy and Petrology, 167, 958.
- 461 Lenaz, D., Youbi, N., De Min, A., Boumehdi, M.A. and Ben Abbou, M. (2014c) Low intra-  
462 crystalline closure temperatures of Cr-bearing spinels from the mantle xenoliths of  
463 the Middle Atlas Neogene-Quaternary Volcanic Field (Morocco): A mineralogical

- 464 evidence of a cooler mantle beneath the West African Craton. American  
465 Mineralogist, 99, 267–275.
- 466 Lenaz, D., Princivalle, F., and Schmitz, B. (2015) First crystal-structure determination of  
467 chromites from an acapulcoite and ordinary chondrites. Mineralogical Magazine, 79,  
468 755–765.
- 469 Lucchesi, S., Della Giusta, A., Russo, U. (1998a): Cation distribution in natural Zn-aluminate  
470 spinels. Mineralogical Magazine, 62, 41–54.
- 471 Lucchesi, S., Amoriello, M., and Della Giusta, A. (1998b) Crystal chemistry of spinels from  
472 xenoliths of the Alban Hills volcanic region. European Journal of Mineralogy, 10,  
473 473–482.
- 474 Lucchesi, S., Bosi, F., and Pozzuoli, A. (2010) Geothermometric study of Mg-rich spinels  
475 from the Somma-Vesuvius volcanic complex (Naples, Italy). American  
476 Mineralogist, 95, 617–621.
- 477 Lutz, H.D., Partik, M., and Sassmannshausen, M. (2000) True Space Group of Spinel-Type  
478 Chromium Oxides and Sulfides, and Ternary Lithium Chlorides - Band Structure  
479 Calculations. Zeitschrift für Kristallographie, 215, 523–528
- 480 Martignago, F., Dal Negro, A., and Carbonin, S. (2003) How  $\text{Cr}^{3+}$  and  $\text{Fe}^{3+}$  affect Mg-Al  
481 order-disorder transformation at high temperature in natural spinels. Physics and  
482 Chemistry of Minerals, 30, 401–408.
- 483 Martignago F., Andreozzi G.B., Dal Negro A. (2006). Thermodynamics and kinetics of  
484 cation ordering in some natural and synthetic  $\text{Mg}(\text{Al},\text{Fe}^{3+})_2\text{O}_4$  spinels from in situ  
485 HT X-ray diffraction. American Mineralogist, 91, 306–312.
- 486 Millard, R.L., Peterson, R.C., and Hunter, B.K. (1992) Temperature dependence of cation  
487 disorder in  $\text{MgAl}_2\text{O}_4$  spinel using  $^{27}\text{Al}$  and  $^{17}\text{O}$  magic-angle spinning NMR.  
488 American Mineralogist, 77, 44–52.
- 489 Nell, J., Wood, B.J., and Mason, T.O. (1989) High temperature cation distributions in  $\text{Fe}_3\text{O}_4$ -  
490  $\text{MgAl}_2\text{O}_4$ - $\text{MgFe}_2\text{O}_4$ - $\text{FeAl}_2\text{O}_4$  spinels from thermopower measurements American  
491 Mineralogist, 74, 339–351.
- 492 Nestola, F., Boffa Ballaran, T., Balic-Zunic, T., Princivalle, F., Secco, L., and Dal Negro, A.  
493 (2007) Comparative compressibility and structural behavior of spinel  $\text{MgAl}_2\text{O}_4$  at  
494 high pressures: the independency on the degree of cation order. American  
495 Mineralogist, 92, 1838–1843.
- 496 Nestola, F., Smyth, J.R., Parisatto, M., Secco, L., Princivalle, F., Bruno, M., Prencipe, M., and  
497 Dal Negro, A. (2009) Effects of non-stoichiometry on the spinel structure at high

- 498 pressure: Implications for Earth's mantle mineralogy. *Geochimica et Cosmochimica*  
499 *Acta*, 73, 489–492.
- 500 Nestola, F., Periotto, B., Andreozzi, G.B., Bruschini, E., and Bosi, F. (2014) Pressure-volume  
501 equation of state for chromite and magnesiochromite: A single-crystal X-ray  
502 diffraction investigation. *American Mineralogist*, 99, 1248–1253.
- 503 North, A.C.T., Phillips, D.C., and Mathews, F.S. (1968) A semi-empirical method of  
504 absorption correction. *Acta Crystallographica*, A24, 351–359.
- 505 O'Neill, H.St.C. and Navrotsky, A. (1984) Cation distribution and thermodynamic properties  
506 of binary spinel solid solutions. *American Mineralogist*, 69, 733–753.
- 507 O'Neill, H.St.C., and Dollase, W.A. (1994) Crystal structures and cation distributions in  
508 simple spinels from powder XRD structural refinements:  $\text{MgCr}_2\text{O}_4$ ,  $\text{ZnCr}_2\text{O}_4$ ,  $\text{Fe}_3\text{O}_4$   
509 and the temperature dependence of the cation distribution in  $\text{ZnAl}_2\text{O}_4$ . *Physics and*  
510 *Chemistry of Minerals*, 20, 541–555.
- 511 O'Neill, H.St.C., Annersten, H., and Virgo, D. (1992) The temperature dependence of the  
512 cation distribution in magnesioferrite ( $\text{MgFe}_2\text{O}_4$ ) from powder XRD structural  
513 refinements and Mössbauer spectroscopy. *American Mineralogist*, 77, 725–740.
- 514 Palin, E.J. and Harrison, R.J. (2007) A computational investigation of cation ordering  
515 phenomena in the binary spinel system  $\text{MgAl}_2\text{O}_4$ - $\text{FeAl}_2\text{O}_4$ . *Mineralogical Magazine*,  
516 71, 611–624.
- 517 Papike, J.J., Burger, P.V., Bell, A.S., Shearer, C.K., Le, L., and Jones, J. (2015) Normal to  
518 inverse transition in martian spinel: Understanding the interplay between chromium,  
519 vanadium, and iron valence state partitioning through a crystal-chemical lens.  
520 *American Mineralogist*, 100, 2018–2025.
- 521 Perinelli, C., Bosi, F., Andreozzi, G.B., Conte, A.M., Armienti, P. (2014) Geothermometric  
522 study of Cr-spinels of peridotite mantle xenoliths from northern Victoria Land  
523 (Antarctica). *American Mineralogist* 99, 839–846.
- 524 Peterson, R.C., Lager, G.A., and Hitterman, R.L., (1991) A time-offlight neutron powder  
525 diffraction study of  $\text{MgAl}_2\text{O}_4$  at temperatures up to 1273 K. *American Mineralogist*,  
526 76, 1455–1458.
- 527 Pouchou, J.L. and Pichoir, F. (1984) A new model for quantitative X-ray micro-analysis. I.  
528 Application to the analysis of homogeneous samples. *La Recherche Aérospatiale*, 3,  
529 13–36.

- 530 Princivalle, F., Della Giusta, A., and Carbonin, S. (1989) Comparative crystal chemistry of  
531 spinels from some suites of ultramafic rocks. *Mineralogy and Petrology*, 40, 117–  
532 126
- 533 Princivalle, F., Della Giusta, A., De Min, A., and Piccirillo, E.M. (1999) Crystal chemistry  
534 and significance of cation ordering in Mg-Al rich spinels from high-grade hornfels  
535 (Pedrazzo-Monzoni, NE Italy). *Mineralogical Magazine*, 63, 257–262.
- 536 Princivalle, F., Martignago, F., and Dal Negro, A. (2006) Kinetics of cation ordering in  
537 natural  $\text{Mg}(\text{Al}, \text{Cr}^{3+})_2\text{O}_4$  spinels. *American Mineralogist*, 91, 313–318.
- 538 Princivalle, F., Martignago, F., Nestola, F., and Dal Negro, A. (2012) Kinetics of cation  
539 ordering in synthetic  $\text{Mg}(\text{Al}, \text{Fe}^{3+})_2\text{O}_4$  spinels. *European Journal of Minerals*, 24,  
540 633–643.
- 541 Redfern, S.A.T., Harrison, R.J., O'Neill, H.St.C., and Wood, D.R.R. (1999) Thermodynamics  
542 and kinetics of cation ordering in  $\text{MgAl}_2\text{O}_4$  spinel up to 1600 °C from in situ neutron  
543 diffraction. *American Mineralogist*, 84, 299–310.
- 544 Righter, K., Sutton, S.R., Newville, M., Le, L., Schwandt, C.S., Uchida, H., Lavina, B., and  
545 Downs, R.T. (2006) An experimental study of the oxidation state of vanadium in  
546 spinel and basaltic melt with implication for the origin of planetary basalt. *American*  
547 *Mineralogist*, 91, 1643–1656.
- 548 Sheldrick, G.M. (2013) SHELXL2013. University of Göttingen, Germany.
- 549 Sickafus, K.E., Wills, J.M. and Grimes, N.W. (1999) Structure of Spinel. *Journal of the*  
550 *American Ceramic Society*, 82, 3279–3292.
- 551 Stachel, T., and Harris, J.W. (2008) The origin of cratonic diamonds - constraints from  
552 mineral inclusions. *Ore Geology Reviews*, 34, 5–32.
- 553 Uchida, H., Lavina, B., Downs, R.T., and Chesley, J. (2005) Single-crystal X-ray diffraction  
554 of spinels from the San Carlos Volcanic Field, Arizona: Spinel as a geothermometer.  
555 *American Mineralogist*, 90, 1900–1980.
- 556 Waerenborgh, J.C., Figueiredo, M.O., Cabral, J.M.P., and Pereira, L.C.J. (1994a) Powder  
557 XRD structure refinements and  $^{57}\text{Fe}$  Mössbauer effect study of synthetic  
558  $\text{Zn}_{1-x}\text{Fe}_x\text{Al}_2\text{O}_4$  ( $0 < x \leq 1$ ) spinels annealed at different temperatures. *Physics and*  
559 *Chemistry of Minerals*, 21, 460-468.
- 560 Waerenborgh, J.C., Figueiredo, M.O., Cabral, J.M.P., and Pereira, L.C.J. (1994b)  
561 Temperature and composition dependence of the cation distribution in synthetic  
562  $\text{ZnFe}_y\text{Al}_{2-y}\text{O}_4$  ( $0 \leq y \leq 1$ ) spinels. *Journal of Solid State Chemistry*, 111, 300-309.

563

564

565 **LIST OF TABLES**

566 **TABLE 1.** Selected X-ray diffraction data for the MgAl<sub>2</sub>O<sub>4</sub>-MgCr<sub>2</sub>O<sub>4</sub> spinels series studied

567 **TABLE 2.** Chemical composition of the MgAl<sub>2</sub>O<sub>4</sub>-MgCr<sub>2</sub>O<sub>4</sub> spinels series studied

568 **TABLE 3.** Observed and calculated crystal-chemical parameters for the MgAl<sub>2</sub>O<sub>4</sub>-MgCr<sub>2</sub>O<sub>4</sub>  
569 spinels series studied (on deposit)

570 **TABLE 4.** Empirical structural formulae (apfu), thermodynamic data (kJmol<sup>-1</sup>) and closure  
571 temperatures (°C) for the MgAl<sub>2</sub>O<sub>4</sub>-MgCr<sub>2</sub>O<sub>4</sub> spinels series studied

572

573

574

575 **LIST OF FIGURES AND FIGURE CAPTIONS**

576 **FIGURE 1.** Variations in the unit cell *a*-parameter versus Cr content in the MgAl<sub>2</sub>O<sub>4</sub>-MgCr<sub>2</sub>O<sub>4</sub>  
577 spinel series studied. Filled circles: samples from this study; filled square: Nestola  
578 et al. (2014). The symbol size is proportional to the analytical error. Dashed line is  
579 linear regressions.

580 **FIGURE 2.** Variations in the unit cell *a*-parameter versus bond distances (T-O and M-O) in the  
581 MgAl<sub>2</sub>O<sub>4</sub>-MgCr<sub>2</sub>O<sub>4</sub> spinel series studied. Circles: samples from this study; squares:  
582 Nestola et al. (2014). The symbol size is proportional to the analytical error. The  
583 dashed line are non-linear regressions.

584 **FIGURE 3.** Plot of the T-site preference of Al in the MgAl<sub>2</sub>O<sub>4</sub>-MgCr<sub>2</sub>O<sub>4</sub> spinel series studied  
585 expressed as <sup>T</sup>Al/Al<sub>tot</sub> against Cr. Filled circles: samples from this study; filled  
586 square: Nestola et al. (2014); filled triangles: Lavina et al. (2003). The horizontal  
587 dashed lines represent inversion of a constant percentage of Al along the series. The  
588 solid lines are linear regression.

589 **FIGURE 4.** Plot of the inversion **(a)** and <sup>T</sup>Al/Al<sub>tot</sub> **(b)** values derived from the O'Neill-  
590 Navrotsky thermodynamic model with  $\alpha_{\text{Mg-Al}} = 23 \text{ kJmol}^{-1}$  and  $\beta_{\text{Mg-Al}} = 13 \text{ kJmol}^{-1}$   
591 (crosses) and from crystal-chemical data (filled circles) against Cr. Solid line is a  
592 guide for the eye. Dashed line represents inversion of a constant percentage of Al  
593 along the series. See text for details on the thermodynamic model.

594 **FIGURE 5.** Plot of closure temperature (*T<sub>c</sub>*) against Cr content for the MgAl<sub>2</sub>O<sub>4</sub>-MgCr<sub>2</sub>O<sub>4</sub>  
595 spinel series studied. Dashed line represents the expected *T<sub>c</sub>*.

**TABLE 1.** Selected X-ray diffraction data for the MgAl<sub>2</sub>O<sub>4</sub>-MgCr<sub>2</sub>O<sub>4</sub> spinels series studied

Crystal	MC02bb	MC02de	MgCr5c	MC10db	MC15ad	MC15aa	MgCr20	MgCr25	MC50b
Instrument	Siemens P4	Siemens P4	APEX-II	Siemens P4	Siemens P4	Siemens P4	APEX-II	APEX-II	Siemens P4
Crystal size (mm)	0.20×0.22×0.23	0.20×0.23×0.23	0.08×0.09×0.10	0.22×0.25×0.29	0.18×0.22×0.26	0.20×0.21×0.24	0.09×0.09×0.10	0.09×0.10×0.10	0.22×0.25×0.27
<i>a</i> (Å)	8.0924(6)	8.1044(4)	8.1539(4)	8.2085(5)	8.2176(5)	8.2376(6)	8.2808(3)	8.2933(3)	8.3244(4)
<i>u</i>	0.26214(4)	0.26232(4)	0.26212(6)	0.26223(8)	0.26227(6)	0.26208(7)	0.26171(6)	0.26164(7)	0.26134(8)
T-O (Å)	1.9222(5)	1.9276(6)	1.9366(8)	1.9511(12)	1.9538(9)	1.9559(10)	1.9609(7)	1.9627(10)	1.9658(11)
M-O (Å)	1.9299(3)	1.9314(3)	1.9447(4)	1.9569(6)	1.9588(5)	1.9649(5)	1.9780(4)	1.9815(5)	1.9912(6)
T-m.a.n.	12.23(5)	12.23(6)	12.07(6)	11.95(12)	12.00(10)	12.10(10)	12.00(7)	12 <sup>a</sup>	12.10(15)
M-m.a.n.	12.99(4)	13.57(4)	15.82(6)	18.21(16)	18.78(13)	19.64(16)	21.67(17)	22.26(22)	23.52(19)
T- <i>U</i> <sup>11</sup> (Å <sup>2</sup> )	0.0050(1)	0.0043(1)	0.0058(2)	0.0072(2)	0.0059(2)	0.0055(2)	0.0055(2)	0.0056(2)	0.0046(2)
M- <i>U</i> <sup>11</sup> (Å <sup>2</sup> )	0.00449(9)	0.00322(9)	0.0052(1)	0.0061(1)	0.00478(9)	0.00432(9)	0.00419(7)	0.0042(1)	0.00313(9)
M- <i>U</i> <sup>12</sup> (Å <sup>2</sup> )	-0.00019(4)	-0.00022(5)	-0.00014(6)	-0.00031(4)	-0.00024(4)	-0.00023(5)	-0.00021(3)	-0.00022(3)	-0.00016(4)
O- <i>U</i> <sup>11</sup> (Å <sup>2</sup> )	0.0081(1)	0.0070(1)	0.0083(2)	0.0091(2)	0.0073(2)	0.0068(2)	0.0058(2)	0.0057(2)	0.0042(2)
O- <i>U</i> <sup>12</sup> (Å <sup>2</sup> )	0.00019(7)	-0.00012(9)	-0.0002(1)	-0.0003(1)	-0.0006(1)	-0.0006(1)	-0.00040(9)	-0.0002(1)	-0.0002(1)
Reciprocal range <i>hkl</i>	0 ≤ <i>h</i> ≤ 16 0 ≤ <i>k</i> ≤ 16 0 ≤ <i>l</i> ≤ 16	0 ≤ <i>h</i> ≤ 16 0 ≤ <i>k</i> ≤ 16 0 ≤ <i>l</i> ≤ 16	-12 ≤ <i>h</i> ≤ 13 -9 ≤ <i>k</i> ≤ 13 -12 ≤ <i>l</i> ≤ 13	0 ≤ <i>h</i> ≤ 16 0 ≤ <i>k</i> ≤ 16 0 ≤ <i>l</i> ≤ 16	0 ≤ <i>h</i> ≤ 16 0 ≤ <i>k</i> ≤ 16 0 ≤ <i>l</i> ≤ 16	0 ≤ <i>h</i> ≤ 17 0 ≤ <i>k</i> ≤ 17 0 ≤ <i>l</i> ≤ 17	-16 ≤ <i>h</i> ≤ 16 -15 ≤ <i>k</i> ≤ 10 -12 ≤ <i>l</i> ≤ 16	-16 ≤ <i>h</i> ≤ 16 -15 ≤ <i>k</i> ≤ 15 -9 ≤ <i>l</i> ≤ 13	0 ≤ <i>h</i> ≤ 17 0 ≤ <i>k</i> ≤ 17 0 ≤ <i>l</i> ≤ 17
No. reflections	624	624	1814	639	639	653	2685	2276	672
No. unique reflections	147	147	84	151	151	155	140	140	158
No. refined parameters	10	10	9	10	10	10	10	9	10
EXTI	0.0053(4)	0.0039(9)	0 <sup>a</sup>	0.006(2)	0.0040(8)	0.0044(8)	0.0024(4)	0.0025(6)	0.0095(9)
<i>R</i> int. (%)	2.27	2.52	2.00	1.82	1.89	2.77	1.46	1.15	3.37
<i>R</i> 1 (%) all reflections	1.36	1.86	0.99	2.40	1.70	1.94	1.17	1.48	1.76
<i>wR</i> 2 (%)	2.60	3.30	2.23	6.04	4.28	3.96	2.79	4.13	3.99
Goof	1.248	1.189	1.263	1.203	1.135	1.136	1.201	1.188	1.122
Diff. Peaks (± <i>e</i> /Å <sup>3</sup> )	-0.20; 0.26	-0.58; 0.24	-0.12; 0.15	-0.45; 0.76	-0.53; 0.48	-0.52; 0.46	-0.41; 0.34	-0.73; 0.48	-0.82; 0.58

Notes: *a* = unit-cell parameter; *u* = oxygen fractional coordinate; T-O and M-O = tetrahedral and octahedral bond lengths, respectively; T- and M-m.a.n. = T- and M-mean atomic number; *U*<sup>11</sup> = atomic displacement parameter; *U*<sup>11</sup> = *U*<sup>22</sup> = *U*<sup>33</sup> and *U*<sup>12</sup> = *U*<sup>13</sup> = *U*<sup>23</sup> (= 0 for T-site due to symmetry reasons); EXTI = extinction parameter; *R* int. = merging residual value; *R*1 = discrepancy index, calculated from *F*-data; *wR*2 = weighted discrepancy index, calculated from *F*<sup>2</sup>-data; GooF = goodness of fit; Diff. Peaks = maximum and minimum residual electron density. Radiation, Mo-*K*α = 0.71073 Å. Data collection temperature = 293 K. Range for data collection 8° < 2θ < 91° (< 72° for sample MgCr5c). Origin fixed at  $\bar{3}m$ . Space group *Fd* $\bar{3}m$ . *Z* = 8. Spinel structure has cations at Wyckoff positions 8a ≡ T (1/8, 1/8, 1/8) and 16d ≡ M (1/2, 1/2, 1/2), and oxygen anions at 32e (*u*, *u*, *u*).

<sup>a</sup> Fixed in the final stages of refinement.

**TABLE 2.** Chemical composition of the MgAl<sub>2</sub>O<sub>4</sub>-MgCr<sub>2</sub>O<sub>4</sub> spinels series studied

Crystal	MC02bb	MC02de	MgCr5c	MC10db	MC15ad	MC15aa	MgCr20	MgCr25	MC50b
Cr <sub>2</sub> O <sub>3</sub> (wt%)	4.90(46)	10.33(1.10)	26.20(9)	47.68(1.33)	50.34(1.05)	53.75(1.32)	66.04(2)	68.86(17)	76.09(14)
Al <sub>2</sub> O <sub>3</sub>	67.43(36)	60.91(1.02)	48.26(23)	29.25(1.40)	25.78(1.03)	22.26(1.20)	11.73(13)	9.44(40)	2.00(3)
MgO	27.89(5)	26.85(29)	26.03(1)	24.47(46)	24.05(42)	23.66(22)	22.06(10)	22.09(1)	21.34(9)
Total	100.21	98.10	100.49	101.40	100.17	99.67	99.83	100.38	99.43
Cr <sup>3+</sup> (apfu)	0.093(8)	0.204(20)	0.534(2)	1.042(26)	1.128(21)	1.228(25)	1.583(3)	1.660(10)	1.916(3)
Al	1.908(7)	1.795(19)	1.466(4)	0.953(33)	0.861(26)	0.758(32)	0.419(4)	0.340(12)	0.075(1)
Mg	0.998(5)	1.001(14)	1.000(2)	1.008(22)	1.016(18)	1.020(18)	0.997(3)	1.004(5)	1.013(3)
Total	2.999	3.000	3.000	3.003	3.005	3.007	2.999	3.004	3.004
# epfu from EMPA	39.02	40.25	43.89	49.49	50.46	51.58	55.40	56.31	59.12
# epfu from SREF	38.20	39.37	43.70	48.38	49.55	51.29	55.34	56.52	59.14

Notes : Cations on the basis of 4 oxygen atoms per formula unit (apfu). Digits in parentheses are estimated uncertainties (1 $\sigma$ ): for reported oxide concentrations, they represent standard deviations of several analyses on individual crystals, whereas, for cations, they were calculated according to error propagation theory; epfu = electrons per formula unit.

**TABLE 3** (on deposit). Observed and calculated crystal-chemical parameters for the MgAl<sub>2</sub>O<sub>4</sub>-MgCr<sub>2</sub>O<sub>4</sub> spinels series studied

Crystal	Al (apfu)	Mg (apfu)	Cr (apfu)	<i>a</i> (Å)	<i>u</i>	T-O (Å)	M-O (Å)	T-man	M-man
MC02bb	1.908(7)	0.998(5)	0.093(8)	8.0924(6)	0.26214(4)	1.9222(5)	1.9299(3)	12.23(5)	12.99(4)
	1.942	0.999	0.059	8.0933	0.26213	1.9223	1.9301	12.23	13.21
MC02de	1.795(19)	1.001(14)	0.204(20)	8.1044(4)	0.26232(4)	1.9276(6)	1.9314(3)	12.23(6)	13.57(4)
	1.861	1.000	0.139	8.1044	0.26232	1.9276	1.9314	12.20	13.66
MgCr05	1.466(4)	1.000(2)	0.534(2)	8.1539(4)	0.26212(6)	1.9366(8)	1.9447(4)	12.07(6)	15.82(6)
	1.466	1.000	0.534	8.1538	0.26217	1.9372	1.9443	12.15	15.86
MC10db	0.953(33)	1.008(22)	1.042(26)	8.2085(5)	0.26223(8)	1.9511(12)	1.9569(6)	11.95(12)	18.21(16)
	1.027	1.000	0.973	8.2088	0.26222	1.9511	1.9570	12.08	18.31
MC15ad	0.861(26)	1.016(18)	1.128(21)	8.2176(5)	0.26227(6)	1.9538(9)	1.9588(5)	12.00(10)	18.78(13)
	0.951	1.000	1.049	8.2182	0.26226	1.9538	1.9590	12.06	18.74
MC15aa	0.758(32)	1.020(18)	1.228(25)	8.2376(6)	0.26208(7)	1.9559(10)	1.9649(5)	12.00(10)	19.64(16)
	0.794	1.000	1.206	8.2378	0.26208	1.9559	1.9650	12.05	19.61
MgCr20	0.419(4)	0.997(4)	1.583(3)	8.2808(3)	0.26171(5)	1.9609(7)	1.9780(4)	12.00(7)	21.67(17)
	0.425	0.998	1.576	8.2816	0.26169	1.9608	1.9783	12.02	21.66
MgCr25	0.340(12)	1.004(5)	1.660(10)	8.2933(3)	0.26164(7)	1.9627(10)	1.9815(5)	12	22.26(22)
	0.344	1.000	1.656	8.2934	0.26164	1.9627	1.9815	12.02	22.10
MC50b	0.075(1)	1.013(3)	1.916(3)	8.3244(4)	0.26134(8)	1.9658(11)	1.9912(6)	12.10(15)	23.52(19)
	0.077	0.999	1.924	8.3253	0.26131	1.9656	1.9916	12.00	23.58

Note: Standard errors in brackets

**TABLE 4.** Empirical structural formulae (apfu), thermodynamic data ( $\text{kJmol}^{-1}$ ) and closure temperatures ( $^{\circ}\text{C}$ ) of the  $\text{MgAl}_2\text{O}_4$ - $\text{MgCr}_2\text{O}_4$  spinels series studied

Crystal	Structural formula	$\alpha_{\text{Mg-Al}}$	$T_c$
MC02bb	$^{\text{T}}(\text{Mg}_{0.773}\text{Al}_{0.227})_{\Sigma 1.000}^{\text{M}}(\text{Mg}_{0.226}\text{Al}_{1.715}\text{Cr}_{0.059})_{\Sigma 2.000} \text{O}_4$	23	805
MC02de	$^{\text{T}}(\text{Mg}_{0.800}\text{Al}_{0.200})_{\Sigma 1.000}^{\text{M}}(\text{Mg}_{0.200}\text{Al}_{1.661}\text{Cr}_{0.139})_{\Sigma 2.000} \text{O}_4$	26	778
MgCr5c	$^{\text{T}}(\text{Mg}_{0.850}\text{Al}_{0.150})_{\Sigma 1.000}^{\text{M}}(\text{Mg}_{0.150}\text{Al}_{1.316}\text{Cr}_{0.534})_{\Sigma 2.000} \text{O}_4$	31	824
MC10db	$^{\text{T}}(\text{Mg}_{0.923}\text{Al}_{0.077})_{\Sigma 1.000}^{\text{M}}(\text{Mg}_{0.077}\text{Al}_{0.950}\text{Cr}_{0.973})_{\Sigma 2.000} \text{O}_4$	43	805
MC15ad	$^{\text{T}}(\text{Mg}_{0.937}\text{Al}_{0.063})_{\Sigma 1.000}^{\text{M}}(\text{Mg}_{0.062}\text{Al}_{0.889}\text{Cr}_{1.049})_{\Sigma 2.000} \text{O}_4$	46	768
MC15aa	$^{\text{T}}(\text{Mg}_{0.948}\text{Al}_{0.052})_{\Sigma 1.000}^{\text{M}}(\text{Mg}_{0.052}\text{Al}_{0.742}\text{Cr}_{1.206})_{\Sigma 2.000} \text{O}_4$	48	786
MgCr20	$^{\text{T}}(\text{Mg}_{0.975}\text{Al}_{0.025})_{\Sigma 1.000}^{\text{M}}(\text{Mg}_{0.023}\text{Al}_{0.400}\text{Cr}_{1.577})_{\Sigma 2.000} \text{O}_4$	57	819
MgCr25	$^{\text{T}}(\text{Mg}_{0.983}\text{Al}_{0.017})_{\Sigma 1.000}^{\text{M}}(\text{Mg}_{0.017}\text{Al}_{0.327}\text{Cr}_{1.656})_{\Sigma 2.000} \text{O}_4$	62	785
MC50b	$^{\text{T}}(\text{Mg}_{0.999}\text{Al}_{0.001})_{\Sigma 1.000}^{\text{M}}(\text{Mg}_{0.001}\text{Al}_{0.075}\text{Cr}_{1.924})_{\Sigma 2.000} \text{O}_4$	100	637

Notes: T = tetrahedrally-coordinated site; M = octahedrally-coordinated site;  $\alpha_{\text{Mg-Al}}$  = coefficient of the O'Neill & Navrotsky (1983) thermodynamic model;  $T_c$  = closure temperature.

Figure 1

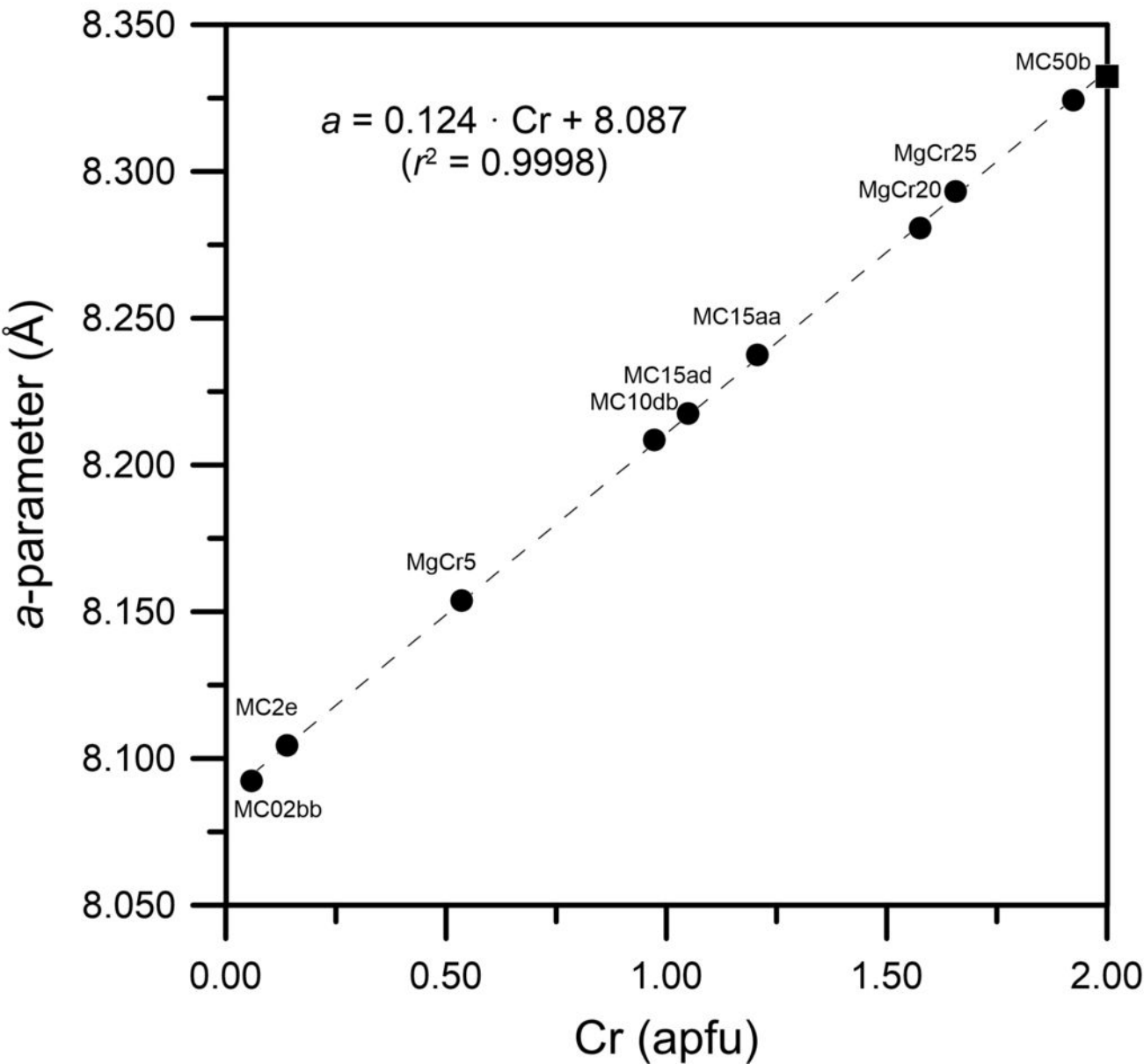


Figure 2

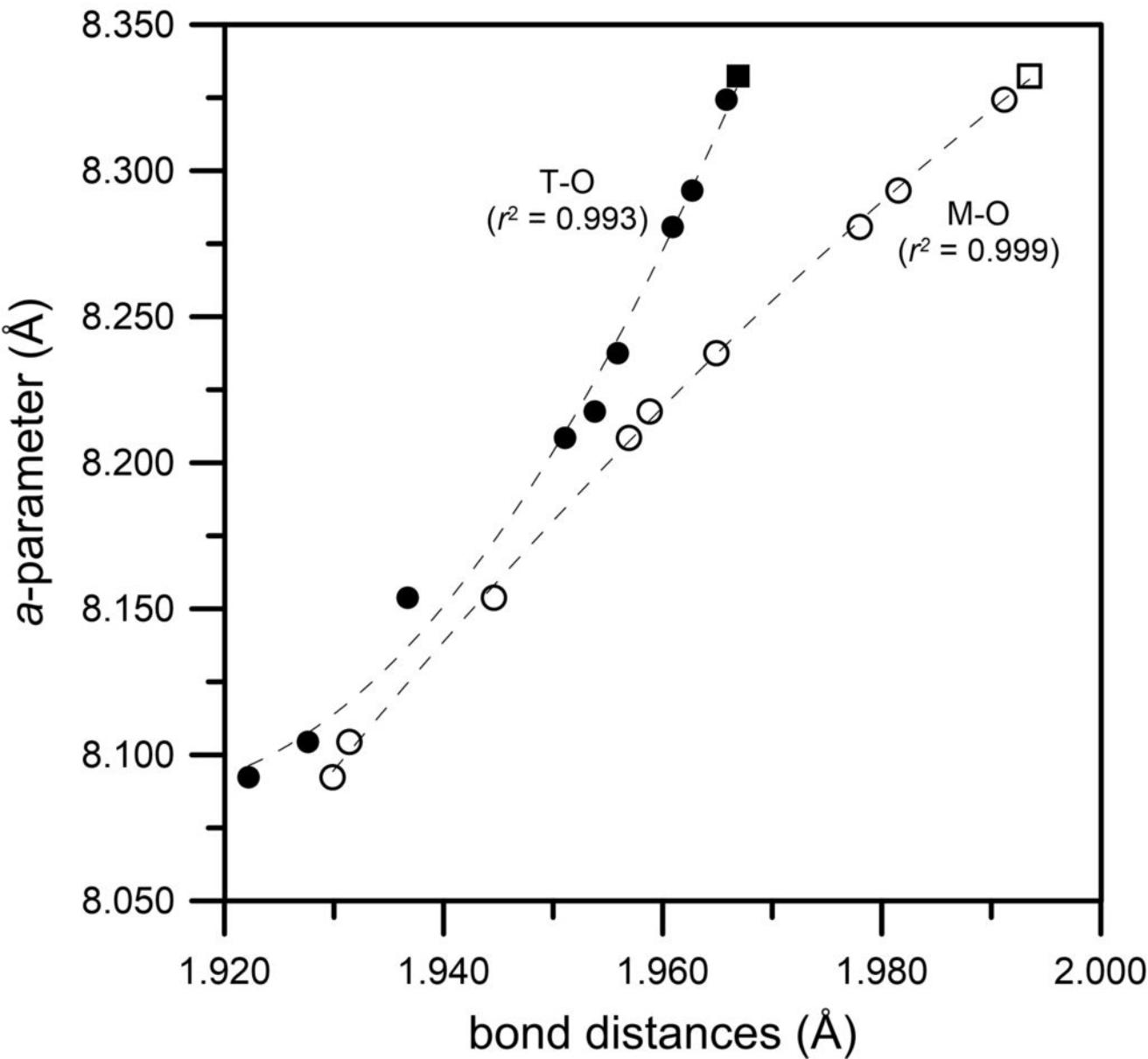


Figure 3

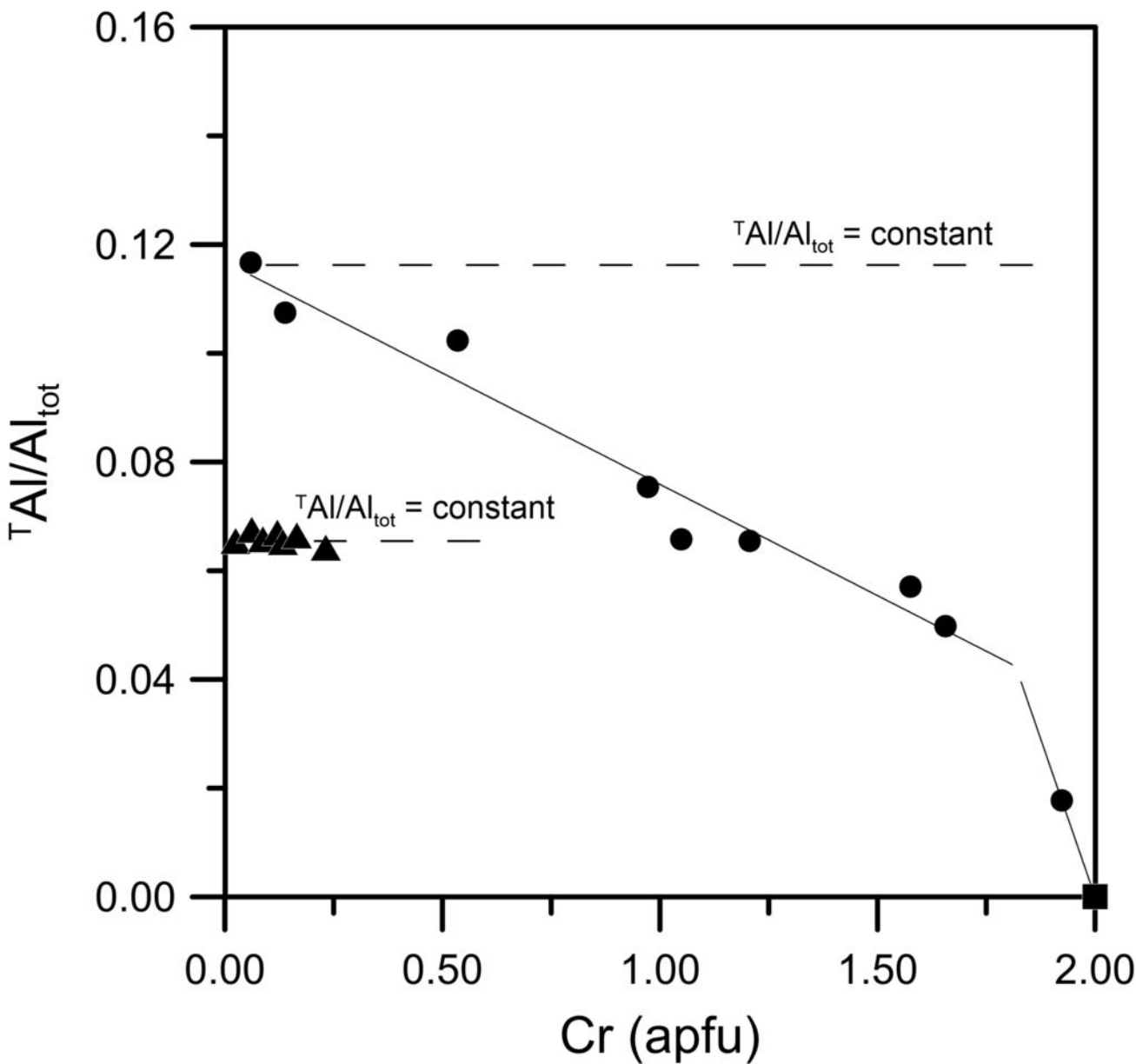


Figure 4

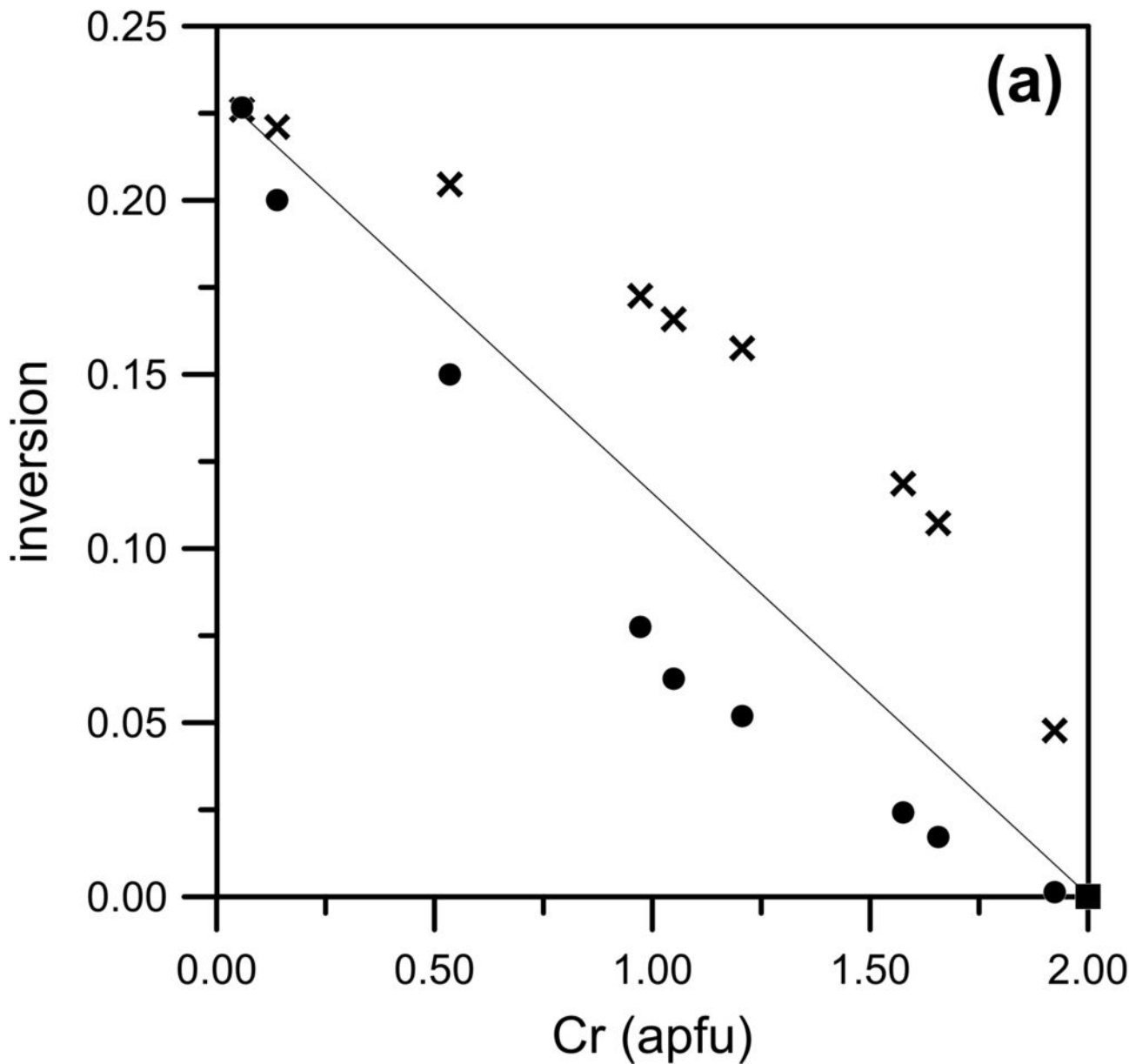


Figure 4

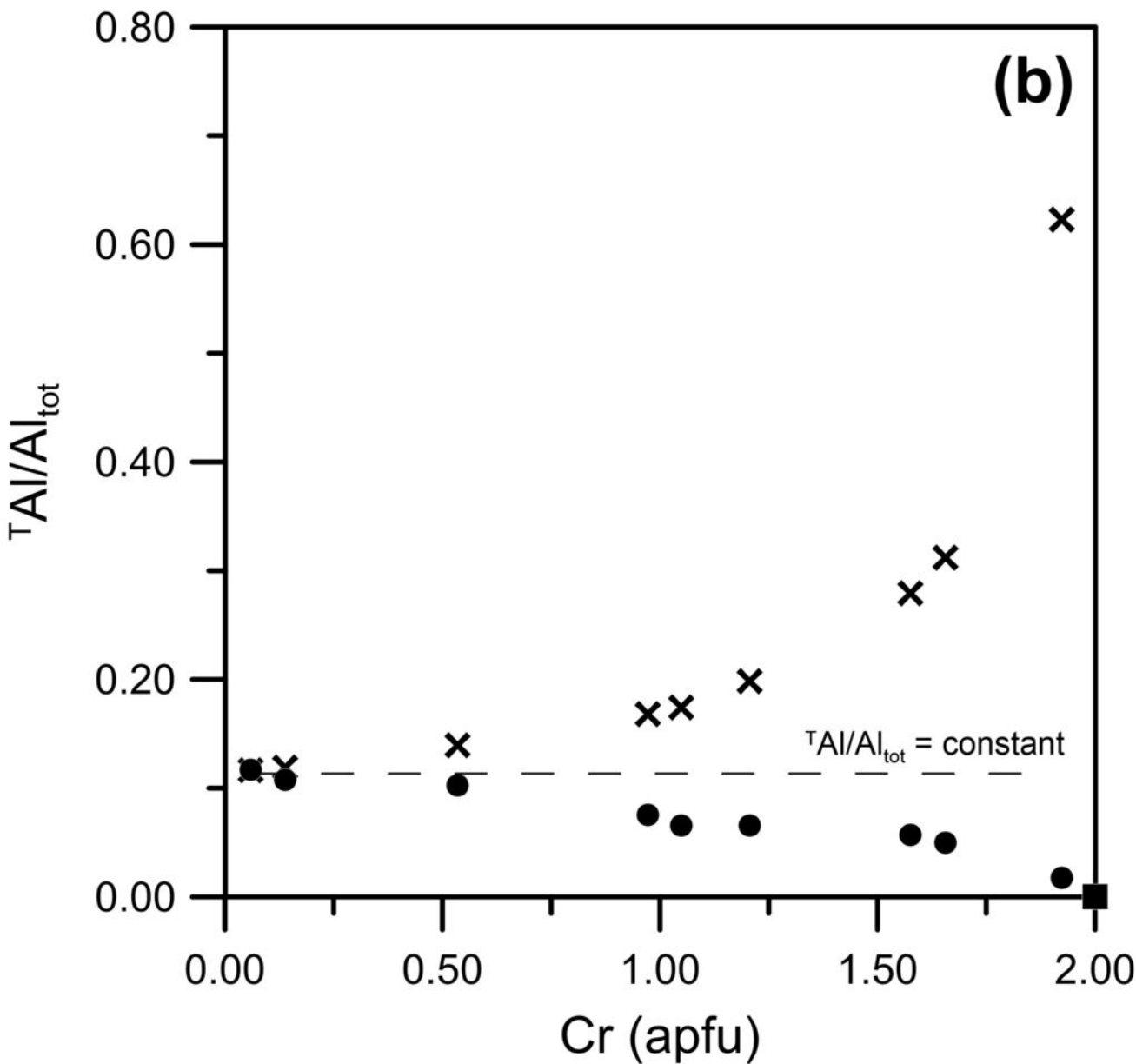


Figure 5

